






## Thermal boundary conductance of artificially and systematically designed grain boundaries of Silicon measured by laser heterodyne photothermal displacement method

T. Harada ; K. Kutsukake ; N. Usami ; T. Ikari ; A. Fukuyama 



*J. Appl. Phys.* 136, 205703 (2024)

<https://doi.org/10.1063/5.0237047>



### Articles You May Be Interested In

Thermophysical property measurement of GaN/SiC, GaN/AlN, and AlN/SiC epitaxial wafers using multi-frequency/spot-size time-domain thermorefectance

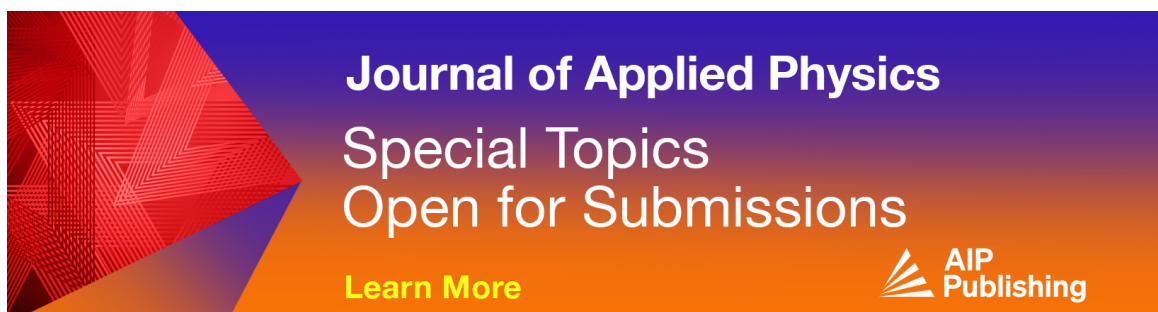
*J. Appl. Phys.* (March 2025)

Lifetime of photoexcited carriers in space-controlled Si nanopillar/SiGe composite films investigated by a laser heterodyne photothermal displacement method

*J. Appl. Phys.* (March 2023)


Study on electrical activity of grain boundaries in silicon through systematic control of structural parameters and characterization using a pretrained machine learning model

*J. Appl. Phys.* (July 2022)



**Journal of Applied Physics**  
Special Topics  
Open for Submissions

[Learn More](#)

# Thermal boundary conductance of artificially and systematically designed grain boundaries of Silicon measured by laser heterodyne photothermal displacement method

Cite as: J. Appl. Phys. **136**, 205703 (2024); doi: [10.1063/5.0237047](https://doi.org/10.1063/5.0237047)

Submitted: 3 September 2024 · Accepted: 12 November 2024 ·

Published Online: 26 November 2024



T. Harada,<sup>1,a)</sup>  K. Kutsukake,<sup>2</sup>  N. Usami,<sup>3</sup>  T. Ikari,<sup>1</sup>  and A. Fukuyama<sup>1</sup> 

## AFFILIATIONS

<sup>1</sup>Faculty of Engineering, University of Miyazaki, Miyazaki 889-2192, Japan

<sup>2</sup>Institute of Materials and Systems for Sustainability, Nagoya University, Nagoya 464-8601, Japan

<sup>3</sup>Graduate School of Engineering, Nagoya University, Nagoya 464-8603, Japan

<sup>a)</sup>Author to whom correspondence should be addressed: [harada.tomoki.q5@cc.miyazaki-u.ac.jp](mailto:harada.tomoki.q5@cc.miyazaki-u.ac.jp)

## ABSTRACT

The overall physical properties of polycrystalline materials vary depending on the microscopic individual grain boundary (GB) properties and their structures. Unlike previous studies that only examined the structure and properties of a specific GB, this study focuses on understanding the thermal boundary conductance (TBC) through artificial and systematic changes in the GB structures. This is achieved by combining an advanced technique to map local thermal expansion displacement using the laser heterodyne photothermal displacement method and a unique crystal growth method that induces spontaneous changes in the GB structures. As a result, we could quantify the TBC of the GB in silicon, considering the changes in three structural parameters of GB: azimuthal misorientation ( $\alpha$ ), asymmetry angle ( $\beta$ ), and deviation angle ( $\theta$ ) from the growth direction. Our findings reveal that the TBC increases with increasing  $\theta$ , whereas parameters  $\alpha$  and  $\beta$  have negligible effects. The underlying physics of this relationship is discussed in terms of local carrier concentration and impurity segregation. These results demonstrate the crucial role of the GB structures in influencing the local TBC, shedding light on potential avenues for enhancing the macroscopic properties of polycrystalline materials by engineering GBs.

© 2024 Author(s). All article content, except where otherwise noted, is licensed under a Creative Commons Attribution-NonCommercial 4.0 International (CC BY-NC) license (<https://creativecommons.org/licenses/by-nc/4.0/>). <https://doi.org/10.1063/5.0237047>

## I. INTRODUCTION

Grain boundaries (GBs) are interfacial defects between two and more crystal grains in a polycrystalline material that affect thermal and electrical transport. Materials, including metals, ceramics, and semiconductors, are widely used as polycrystalline materials. To improve polycrystalline materials, control of GB properties is essential because the microscopic properties of individual GBs and their network determine the macroscopic properties of the entire polycrystalline material.<sup>1–4</sup> In some cases, GB engineering has improved the properties of polycrystalline materials such as stainless steel<sup>5</sup> and ZnO<sup>6</sup> by controlling the GBs. Clarifying the nature of individual GBs in each structure will contribute to GB engineering.

For thermoelectric applications, in which a temperature difference is converted to electricity, materials with high-density GBs are used to reduce thermal conductivity and improve performance.<sup>7,8</sup> Moreover, in the thermal management of electronics, the thermal resistance of GBs must be suppressed to optimize heat dissipation. However, the relationship between thermal properties such as thermal boundary conductance (TBC) and GB structures is not yet clear. Studies have reported on the atomic structure and TBC at GBs using molecular dynamics simulations,<sup>9–12</sup> but there are few examples of experimental TBC measurements. Sakata *et al.* and Xu *et al.* measured the TBC of Si GBs using the frequency-domain thermorefectance and 3-omega methods,<sup>13,14</sup> respectively, while Hurley *et al.*, Tai *et al.*, and Isotta *et al.* measured the TBC of

19 May 2025 10:32:58

Si/SiO<sub>2</sub> interfaces,<sup>15</sup> Al<sub>2</sub>O<sub>3</sub>,<sup>16</sup> and SnTe,<sup>17</sup> respectively. However, these previous studies focused only on one or two types of GBs, and the relationship between systematically prepared GB structures and TBC has not been measured. This is due to the challenges in fabricating samples with systematically altered GB structures and developing a method that can quantify the TBC of such samples. The relationship between GB structures and TBC needs to be investigated systematically to further understand the thermophysical properties of GB.

We fabricated  $\langle 100 \rangle$  or  $\langle 110 \rangle$  oriented crystalline Si crystals with artificially controlled GB planes to systematically investigate the effects of misorientation and asymmetry on their properties.<sup>18</sup> The fabricated GBs were characterized by three parameters: the misorientation angle  $\alpha$  for the  $\Sigma$  values, asymmetric angle  $\beta$ , and deviation angle  $\theta$  from the  $z$  axis, as shown in Fig. 1. We previously investigated the effects of  $\alpha$ ,  $\beta$ , and  $\theta$  on the electrical properties of GBs using photoluminescence imaging and a pretrained machine learning model.<sup>19,20</sup> As a result, we found that a larger  $\theta$  value resulted in a faster boundary recombination velocity; the boundary recombination velocity has a baseline that depends on  $\alpha$ , and its magnitude is smaller at  $\Sigma 5$  GBs than at  $\Sigma 13$  GBs.<sup>20</sup> The technique of fabricating artificially controlled GBs allows us to systematically discuss the relationship between the TBC and GB structures.

We developed a laser heterodyne photothermal displacement (LH-PD) method to measure the nonradiative recombination in semiconductors and their thermophysical properties.<sup>21</sup> The LH-PD method detects the displacement due to thermal expansion caused by excitation beam irradiation. It is highly sensitive, being able to measure displacements as small as 50 pm owing to the heterodyne interferometer used for detection. The position of the excitation and probe beam irradiation can be controlled separately, making it possible to measure the thermal expansion displacement across the GB, as shown in Fig. 1. Because the observed time variation of the

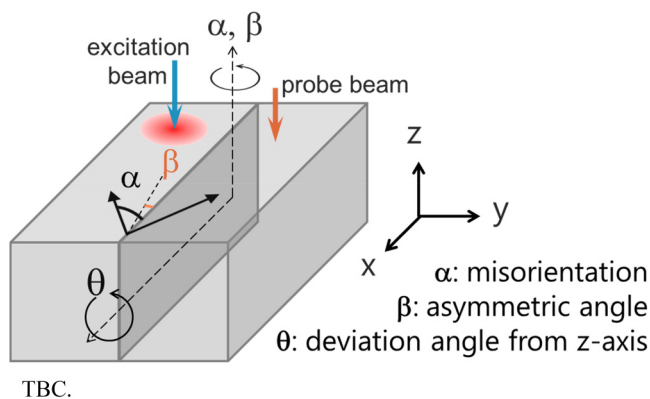


**FIG. 1.** Three parameters of GB structures: misorientation  $\alpha$ , asymmetric angle  $\beta$ , and deviation angle  $\theta$  from the  $z$ -direction. The  $z$ -direction is the direction of growth. Note that oriented GBs have one angle component in misorientation around the oriented  $z$ -direction while general GBs have three angle components in misorientation. The excitation and probe beams can be controlled to irradiate separate positions when using the laser heterodyne photothermal displacement (LH-PD) method, making it possible to measure the signal across the GB.

displacement includes thermophysical properties, the TBC can be obtained by comparing the experimental and numerically calculated time variations of the displacement.

The relationship between the GB structures' parameters ( $\alpha$ ,  $\beta$ , and  $\theta$ ) and TBC can be systematically evaluated by combining the LH-PD method with our crystal growth technique, which allows artificial control of the GB structures. In this study, we prepared samples with systematically varying  $\alpha$ ,  $\beta$ , and  $\theta$  and discussed the relationship between the GB structures and TBC.

## II. MATERIALS AND METHODS

### A. Sample preparation

The crystal growth process is shown in Fig. 2. The designed seed crystal enabled the fabrication of artificially designed GBs. Seed crystal plates ( $2 \times 10 \times 5 \text{ cm}^3$ ) were cut from Czochralski-grown single-crystalline Si ingots with a  $\langle 100 \rangle$  or  $\langle 110 \rangle$  orientation in the  $z$ -direction. Arbitrary GB planes parallel to the  $\langle 100 \rangle$  or  $\langle 110 \rangle$  orientations can be formed in the seed crystals by controlling the cutting plane. The seed crystal, which had four artificial GBs, was placed at the bottom of a quartz crucible coated with a mold-release agent ( $\text{Si}_3\text{N}_4$ ). The semiconductor-grade Si raw materials were placed on the seed crystals. All raw materials and the top 2 cm of the seed crystal were melted by controlling the temperature distribution in the growth direction using three heaters in a crystal growth furnace. The initial solid-liquid interface was controlled in a convex shape. The Si was then solidified, and ingots were grown to maintain the designed GB structures. The fabricated ingot had dimensions of  $10 \times 10 \times 13 \text{ cm}^3$ .

These GBs have three degrees of freedom: the misorientation angle  $\alpha$  defined as the relative crystal orientation around the common axis in the  $z$ -direction; asymmetric angle  $\beta$  from the mirror plane; and deviation angle  $\theta$  from the  $z$ -direction.  $\alpha$  and  $\beta$  are controlled by the cutting plane of the seed crystals as mentioned above. When  $\beta$  is 0, the GB is symmetric; when  $\beta$  is greater than 0, it is asymmetric. On the other hand,  $\theta$  varied owing to the convex shape of the seed crystals. When the seed crystal was convex, the GB plane was tilted to minimize the total free energy. This tilt angle was  $\theta$ . The continuous variation in  $\theta$  during growth

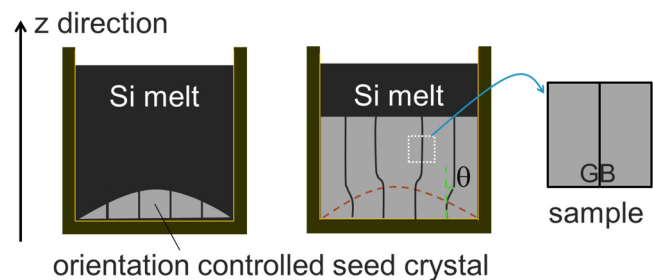


**FIG. 2.** Schematic diagram of the crystal growth process. The  $\alpha$  and  $\beta$  were controlled by the orientation of seed crystals. The solid-liquid interface was convex just before growth began. As a result,  $\theta$  varied. Each sample contained only one GB. Some sample  $\theta$  changed continuously.

19 May 2025 10:32:58

allowed for systematic characterization with a wide range of  $\theta$  values.

The ingots were doped with P during growth, and its concentration varied with the position in the growth direction. The resistivity variation in the area where TBC was measured was 0.76–2.15  $\Omega\text{cm}$ , corresponding to the doping concentration of  $2.2 \times 10^{15}$ – $6.7 \times 10^{15}\text{cm}^{-3}$ . The electrical resistivity was measured using the four-point probe method. Crystal growth and electrical conductivity measurements have been previously explained in detail.<sup>18,20</sup>

Wafers for evaluation were cut from the produced ingot with a size of  $1.0 \times 1.0 \times 0.1\text{cm}^3$  in the plane perpendicular to the bottom of the crucible and the GB plane, with the GB plane in the center as shown in Fig. 2. Each sample contained only one GB. Totally, seven GB samples were prepared from  $\langle 100 \rangle$  or  $\langle 110 \rangle$  ingots as listed in Table I. In addition, a “without GB” sample was also prepared for comparison. Samples A, B, C, and D were prepared to discuss differences due to  $\alpha$ ; samples D, F, and G were prepared to discuss differences due to  $\beta$ ; and samples D and E were prepared to discuss differences due to  $\theta$ . For samples D and E,  $\theta$  varied continuously.

The Al film used to absorb the excitation beam and act as a heat source was fabricated by vacuum evaporation in  $20 \times 20\text{ }\mu\text{m}$  squares using masks fabricated by photolithography. When the excitation beam irradiates the semiconductor surface, photoexcited carriers are generated, making analysis difficult. When the excitation beam irradiates the Al, photoexcited carriers are not generated and become heat sources, which are easier to discuss. The Al film was deposited adjacent to the GB layer. The film formed 5–15  $\mu\text{m}$  away from the GB, as shown in Figs. 3(a) and 3(b), and the distance was confirmed by microscopy. This deviation in distance was due to the precision of the photolithography positioning. The thickness of the Al film was 64 nm, as obtained from a film thickness monitor during evaporation. The distance from one Al film to the other in the in-plane direction of the sample was more than 200  $\mu\text{m}$ . Because the thermal diffusion length in Si and in our experimental setup was approximately 100  $\mu\text{m}$ , a distance of 200  $\mu\text{m}$  was sufficient to ignore the effects of the other Al films.

## B. LH-PD measurement

A schematic of the LH-PD method is shown in Fig. 4. The LH-PD method detected the surface thermal expansion caused by a modulated excitation beam using a heterodyne interferometer.

**TABLE I.** Prepared samples. One GB has three factors  $\alpha$ ,  $\beta$ , and  $\theta$ .

| Sample | z-orientation         | GB planes   | $\Sigma$ value | $\alpha$ (°) | $\beta$ (°) | $\theta$ (°) |
|--------|-----------------------|-------------|----------------|--------------|-------------|--------------|
| A      | $\langle 110 \rangle$ | (552)/(552) | 27a            | 31.6         | 0           | 0            |
| B      | $\langle 110 \rangle$ | (332)/(332) | 11             | 50.5         | 0           | 1            |
| C      | $\langle 100 \rangle$ | (540)/(540) | 41             | 77.3         | 0           | 7            |
| D      | $\langle 100 \rangle$ | (310)/(310) | 5              | 36.9         | 0           | 6–9          |
| E      | $\langle 100 \rangle$ | (310)/(310) | 5              | 36.9         | 0           | 9–14         |
| F      | $\langle 100 \rangle$ | (740)/(810) | 5              | 36.9         | 11.3        | 4            |
| G      | $\langle 100 \rangle$ | (110)/(810) | 5              | 37.9         | 26.1        | 0            |

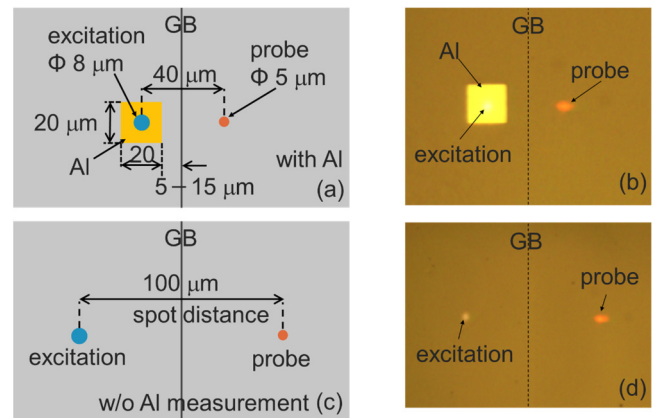


**FIG. 3.** LH-PD measurement setup. The spot distance means the distance between excitation and probe beam irradiation location. (a) and (b) The “with-Al measurement,” in which the Al film that formed adjacent to the GB was irradiated with the excitation beam. (c) and (d) The “w/o-Al measurement,” in which the Si surface was irradiated with the excitation beam. (b) and (d) The optical microscope image for the with-Al or w/o-Al measurement, respectively.

The excitation beam was a continuous-wave laser from a laser diode (LD: 808 nm). The intensity was modulated using an oscillator. The diameter and intensity of the excitation beam were 7.8  $\mu\text{m}$  and  $1.6 \times 10^5\text{ W/cm}^2$ , respectively. A He–Ne laser was used as the probe beam for heterodyne interferometer. The diameter and

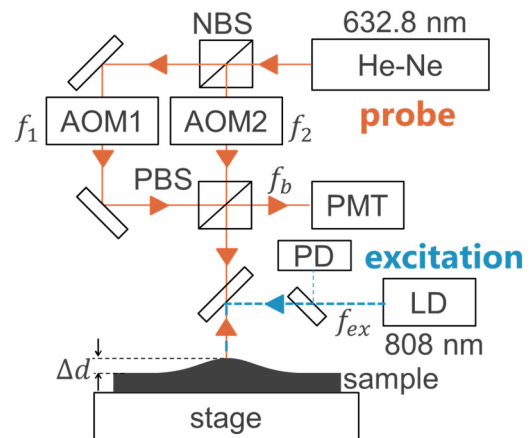


**FIG. 4.** Schematic diagram of the LH-PD measurement. A He–Ne laser was used as the probe beam. A nonpolarized beam splitter (NBS) split the probe beam into two beams. One beam irradiated the sample and was reflected from the surface as the measured beam, whereas the other was a reference beam. A quarter-wave plate and polarizing beam splitter (PBS) merged the measured and reference beams. They formed a beat wave in front of the detector (photomultiplier tube, PMT) because the acousto-optic modulator (AOM) shifted the frequency of each beam. The LH-PD method measures the displacement from the phase shift of the beat wave.

19 May 2025 10:32:58

intensity of the probe beams were  $5.4\text{ }\mu\text{m}$  and  $5.6 \times 10^3\text{ W/cm}^2$ , respectively. The detailed LH-PD method has been previously described.<sup>21</sup>

The LH-PD method performs excitation in two ways. One is to irradiate the excitation beam directly onto the semiconductor surface, and the other is to irradiate a fabricated metal thin film (Al in this case) on the sample. Hereafter, the former is referred to as “w/o-Al measurement” and the latter as “with-Al measurement.” In the w/o-Al measurement, photoexcited carriers are generated and the surface thermally expands owing to nonradiative recombination. In this case, physical properties such as the optical absorption coefficient, thermal diffusivity, carrier lifetime, and carrier mobility must be considered for discussion. In contrast, in the with-Al measurement, since the metal film absorbs the excitation beam, the excitation beam cannot reach the sample, and no photoexcited carriers are generated. In this case, the carrier lifetime and carrier mobility need not be considered because photoexcited carriers are not generated. The number of physical properties to be considered is reduced, which makes the discussion easier. In the with-Al measurements, we can concentrate on the discussion of the thermophysical properties. In this study, both excitation approaches were used to measure the TBC.

The excitation and probe beams can irradiate separate locations and measure the signal across GBs. The distance between the irradiation locations of the excitation and probe beam is hereafter referred to as the “spot distance.” Because the thermal expansion displacement was measured after the generated heat passed through the GB was detected, the measured displacement included information on the TBC at the GB. The experimental arrangements of the excitation beam, probe beam, Al film, and GBs for the with- and w/o-Al measurements are shown in Figs. 3(a)–3(d), respectively. The with-Al film measurements were performed at a spot distance of  $40\text{ }\mu\text{m}$ . Although the distance between the Al film and the GB varied from sample to sample, as mentioned in the last paragraph of Sec. II A, the excitation beam always irradiated the center of the Al film while maintaining a constant spot distance. In contrast, the w/o-Al measurements were performed at a spot distance of  $100\text{ }\mu\text{m}$ . The difference in spot distance between the two measurements is due to two reasons. First, in the with-Al measurement, 87% of the excitation beam is reflected by Al, resulting in less heat transfer and smaller displacement, which allows for a shorter spot distance ( $40\text{ }\mu\text{m}$ ) to maintain a sufficient signal. Second, in the w/o-Al measurement, a shorter spot distance caused measurement inaccuracies due to the thermal lens effect, so a larger spot distance ( $100\text{ }\mu\text{m}$ ) was used to minimize this effect to obtain an appropriate signal intensity. The thermal lens effect is negligible in the with-Al measurement due to lower heat absorption.

The LH-PD method can measure the time variation of displacement. When the TBC at the GB is small, that is, when the GB is less heat-transparent, the decay curve of the time variation of the displacement after the end of the excitation beam irradiation is delayed. The time-variation curve of the displacement was reproduced by numerical calculations, and the TBC was obtained by the fitting procedures. In this study, the time variation of the displacement was measured for 400 000 cycles and averaged. The standard error, which represents the precision of the measurement, was then

calculated. Measurements were made on two sampling points near the designated GB, and the same results were obtained.

The advantages of the LH-PD method over other photothermal conversion-based methods are the possibility of measuring the time variation of displacement, the possibility of changing the spot distance between the excitation and probe beam, and the possibility of estimating thermophysical properties (thermal diffusivity) and carrier properties (carrier lifetime, carrier mobility, and boundary recombination velocity) through numerical calculations described in Sec. II C.<sup>21–24</sup> The advantage of the LH-PD method over the time-domain thermoreflectance and frequency-domain thermoreflectance methods is that it can measure sufficient signal intensity even when the distance between the excitation and probe beams is more than several tens of micrometers.<sup>25</sup> These features allow TBC to be properly measured under two measurement conditions: with-Al and w/o-Al measurements.

### C. Numerical calculations for analysis

To reproduce the displacement of the LH-PD method and obtain the TBC, numerical calculation was performed using COMSOL Multiphysics® software.<sup>26</sup> Numerical calculations were performed with reference to the theoretical calculations for the photoacoustic method considering photoexcited carriers.<sup>27</sup> Because the experimental conditions were different for with- and w/o-Al measurements, appropriate models were prepared and calculated for each measurement. Three-dimensional Cartesian coordinates were considered for both the with- and w/o-Al measurements. The geometry of the calculation model adequately reproduced the shapes of the actual samples. Because the distance from the GB to Al was different for each sample, as mentioned in the last paragraph of Sec. II A, the distance was checked with a microscope, and the calculation model was prepared by appropriately reproducing the distance for each sample. Thus, the fact that the distance between Al and the GB varied from sample to sample did not affect the obtained TBC. Moreover, the spot distance also differed between the with- and w/o-Al measurements but was considered in the calculations.

For the w/o-Al measurement, the carrier continuity, heat, and elastic equations were used to reproduce the thermal displacement. The concentration of the photoexcited carriers was calculated using the carrier continuity equation. The photoexcited carrier distributions were calculated using the optical absorption based on the Lambert–Beer law. The time variation of the excitation beam, measured using a photodiode during the experiment, was considered in the calculations. For the w/o-Al measurements, surface recombination was considered as the boundary condition. In addition,  $v_{GB}$  needed to be considered for the w/o-Al measurement. The  $v_{GB}$  values at the GBs have been previously reported using photoluminescence imaging.<sup>20</sup> Though the  $v_{GB}$  varied with the location in a sample,  $v_{GB}$  was quoted from our previous study and properly considered in the calculation.<sup>20</sup> The surface and boundary recombination were considered as nonradiative recombination and were included in the heat source of the heat equation. Then, the heat equation was solved to calculate the temperature.

For the with-Al measurement, Lambert–Beer’s law, heat equation, and elastic equation were considered. The time variation in

19 May 2025 10:32:58



the excitation beam was used in Lambert–Beer’s law. The absorbed excitation beam was used as the heat source in the heat equation with considering the optical absorption coefficient of Al. The difference between the equations used in the w/o- and with-Al measurements is whether photoexcited carriers are generated. The details of these calculations have been explained previously.<sup>21</sup>

Because the sample was in contact with ambient air, natural convection with air was considered as a boundary condition, and the surface in contact with the sample stage was considered adiabatic because the sample stage was made of quartz glass for the heat equation in both the w/o- and with-Al measurements.

For the with-Al measurements, convection with air was also considered for the Al surface. The temperature distribution in the Al film itself also affected the LH-PD displacement. For instance, heat could accumulate at the edges of the Al film. This effect was considered in the calculations. The boundary condition between Al and Si was the TBC, hereafter referred to as  $TBC_{Al/Si}$ . This was also confirmed for the same wafer sample without a GB. Calculations were performed while varying  $TBC_{Al/Si}$ , and the TBC with the smallest root mean square error between the experiment and calculation was determined to be  $TBC_{Al/Si}$ . The obtained  $TBC_{Al/Si}$  was used to obtain the TBC at the GBs in the calculation for the with-Al measurement.

After temperature distribution was calculated by solving heat equation, the displacement was calculated by considering the thermal strain. The calculations were performed by changing the TBC at the GBs, and the calculated time variation of the displacement was compared to the experimental results. The TBC with the smallest root mean square error between the experiment and calculation was determined as the TBC at the GBs for both the with- and w/o-Al measurements.

Even if the thickness of the grain boundary changes, there is no effect on the calculated TBC if the change is only a few nanometers, which is thin relative to the spot distance. Since the TBC is calculated based on the amount of heat prevented by the GB, the same TBC is estimated when the amount of heat prevented is the same even if the thickness of the GB is different.

The parameters used in these calculations are listed in Table II. For clarity, the physical properties used in the with- and w/o-Al measurements are shown separately. The thermophysical parameters were used for both the with- and w/o-Al measurements, but the parameters related to carriers were used only for the w/o-Al measurement. The carrier lifetimes listed in Table II were estimated using photoluminescence imaging and machine learning<sup>20</sup> through which the carrier diffusion length was also measured. The average calculated carrier diffusion length was  $200\mu\text{m}$ . Because the samples in this study were n-type, minority carrier holes are discussed. The carrier lifetime was estimated from the measured carrier diffusion lengths using the diffusion coefficients of the holes obtained from the previous literature. Thus, the carrier lifetime was estimated to be  $40\mu\text{s}$ .

### III. RESULTS AND DISCUSSION

#### A. With-Al measurement

The time variation in the displacement of the experimental results for the samples with and without GBs is shown in Fig. 5. When the excitation beam was turned on, the displacement started

**TABLE II.** Physical parameters used in the numerical calculations. The optical absorption coefficient of Si and the physical properties related to carrier diffusion and recombination at the bottom of the table are not needed for with-Al measurements.

|  | With-Al measurement |                        | W/o-Al measurement        |
|--|---------------------|------------------------|---------------------------|
|  | Al <sup>28–32</sup> | Si <sup>28,33–35</sup> | Si <sup>20,28,33–35</sup> |
| Optical absorption coefficient at 808 nm $a_{Al}$ or $a_{Si}$ ( $\text{cm}^{-1}$ ) | $1.3 \times 10^6$   | ...                    | 922                       |
| Thermal conductivity $\kappa$ ( $\text{W/mK}$ )                                    | 236                 |                        | 130                       |
| Density $\rho$ ( $\text{g/cm}^3$ )   | 2.7                 |                        | 2.33                      |
| Specific heat $c$ ( $\text{J/gK}$ )  | 0.9                 |                        | 0.713                     |
| Young’s modulus (Gpa)  | 70                  |                        | 130                       |
| Poisson’s ratio  | 0.34                |                        | 0.278                     |
| Linear expansion coefficient ( $\times 10^{-6} \text{K}^{-1}$ )                    | 23.1                |                        | 2.6                       |
| Bandgap energy $E_g$ (eV)  | ...                 | ...                    | 1.12                      |
| Carrier lifetime $\tau$ ( $\mu\text{s}$ )  | ...                 | ...                    | 40                        |
| Hole diffusion coefficient $D$ ( $\text{cm}^2/\text{s}$ )                          | ...                 | ...                    | 10                        |
| Hole mobility ( $\text{cm}^2/\text{Vs}$ )  | ...                 | ...                    | 380                       |
| Boundary recombination velocity $v_{GB}$ ( $\text{cm/s}$ )                         | ...                 | ...                    | 3400–9000                 |
| Surface recombination velocity $v_{SR}$ ( $\text{cm/s}$ )                          | ...                 | ...                    | Changed                   |

to increase, whereas when the excitation beam was turned off, it started to decrease. A difference in the decay curve was observed, and the thermal boundary resistance of the GB delayed the time variation in the displacement, as shown in Fig. 5.

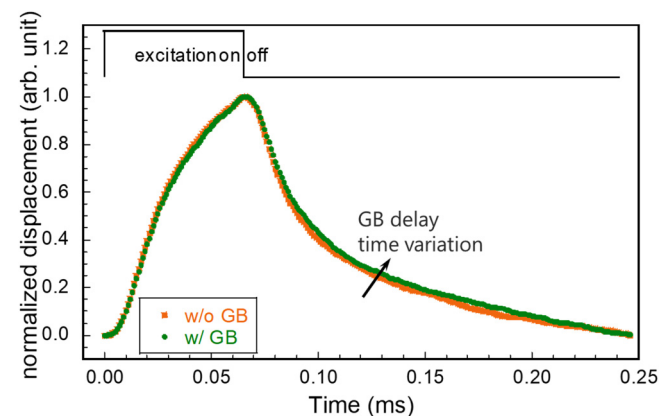


**FIG. 5.** Time variation of displacement with or without GB samples measured using the LH-PD method. The GB delayed the time variation of the displacement. The time variation of the displacement was measured for 400 000 cycles and averaged. Measurements were made on two sampling points near the designated GB, and the same results were obtained.

19 May 2025 10:32:58

The  $TBC_{Al/Si}$  was measured using the experimental results for the sample without a GB, as shown in Fig. 5. Calculations were performed by varying the TBC between Al and Si to determine the TBC that minimized the root mean square error between the experimental and calculated results. As a result, the obtained  $TBC_{Al/Si}$  was  $25 \text{ kW/m}^2\text{K}$ , and this value was used for estimating the TBCs at the GBs. This  $TBC_{Al/Si}$  value was small compared with other reported values.<sup>36</sup> The reported TBC between the Si and Al has been measured using the time-domain thermoreflectance method. This reported  $TBC_{Al/Si}$  was  $13 \text{ MW/m}^2\text{K}$  after considering the  $\text{SiO}_2$  in the natural oxide film on Si. The small  $TBC_{Al/Si}$  is because all the differences between the experiments and calculations, including those unrelated to  $TBC_{Al/Si}$ , were also included in  $TBC_{Al/Si}$ , resulting in a value that differs from those of other reports. The small  $TBC_{Al/Si}$  did not affect the calculation of the TBC at the GB. The reason for this is explained as follows.  $TBC_{Al/Si}$  was estimated using the sample without GB and determined such that the experimental and calculated results agreed for the sample without a GB. The difference between the samples with and without GB was the presence or absence of a GB, that is, the presence or absence of TBC at the GB. Thus, the difference between the experimental results of the samples with and without GBs, as shown in Fig. 5, corresponds to the effect of the TBC at the GB; thus, the TBC at the GB can be estimated. Because of concerns about  $TBC_{Al/Si}$ , w/o-Al measurements were performed to calculate TBC of GBs without  $TBC_{Al/Si}$ , which will be explained in Sec. III B.

An example of the experimental and best-fitted calculation results for the estimation of TBC is shown in Fig. 6. The TBC that

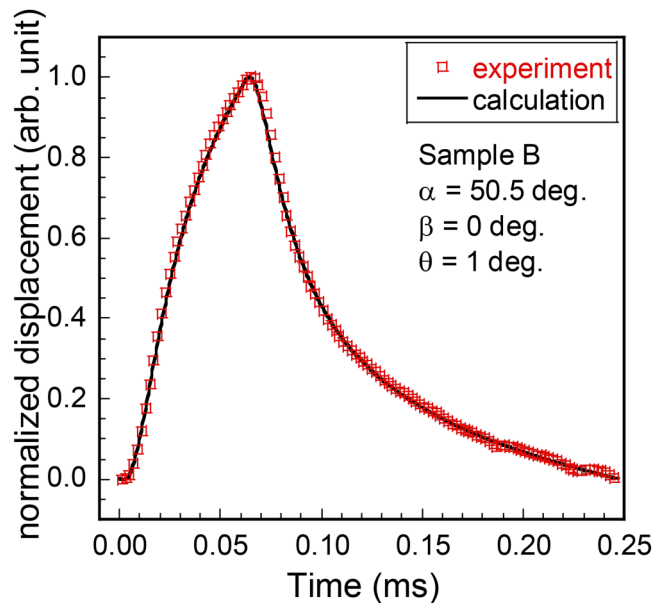


**FIG. 6.** An example of time variation of displacement of experimental (red squares) and best-fitted calculation results (green solid curve). The TBC was estimated by searching for the minimum of the root-mean-square error between experimental and calculation results.

minimized the root mean square error between the experimental and calculated results was sought. The calculation reproduced the experiment. The TBCs obtained for each sample are shown in Fig. 7. The TBCs were independent of  $\alpha$ , as shown in Fig. 7(a). Although  $\alpha$  corresponds to the  $\Sigma$  value, the TBC was found to be independent of the  $\Sigma$  value. The relationship between the  $\Sigma$  value and TBC is shown in a smaller figure in Fig. 7(a). Additionally, the TBC was independent of  $\beta$ , as shown in Fig. 7(b). However, the TBC increased with increasing  $\theta$ , as shown in Fig. 7(c). The parameter affecting the TBC was found to be  $\theta$ .

Nevertheless, as shown in Table I, the samples used to examine the relationship between  $\alpha$ ,  $\beta$ , and the TBC, as shown in Figs. 7(a) and 7(b), also include samples for which  $\theta$  is not zero, such as samples C, D, and F. To simultaneously illustrate the relationships between the three parameters ( $\alpha$ ,  $\beta$ , and  $\theta$ ) and the TBC, a three-dimensional heat map was created, as shown in Fig. 7(d). Figures 7(a)–7(d) are based on the same results. The three-dimensional illustration also shows that a larger  $\theta$  value results in a larger TBC. When preparing the samples before the measurement, we fixed the remaining two parameters to evaluate the influence of one of the three parameters ( $\alpha$ ,  $\beta$ , and  $\theta$ ) and prepared the samples listed in Table I. Consequently, when illustrated in three dimensions, many of the samples had an  $\alpha$  value of  $36.9^\circ$ .

The TBC at the GB was evaluated; however, the  $TBC_{Al/Si}$  was small, as previously mentioned. These results were confirmed by the w/o-Al measurements. Since w/o-Al measurements were performed without the Al film, the effect of  $TBC_{Al/Si}$  could be excluded.

### B. W/o-Al measurement

In the w/o-Al measurement, the excitation beam directly irradiated the Si surface; therefore, there was no need to consider  $TBC_{Al/Si}$ . However, the carrier properties of carrier mobility,  $\tau$ ,  $v_{GB}$ , and  $v_s$ , needed to be considered in the numerical calculations. The literature-based and measured values of carrier mobility,  $\tau$ , and  $v_{GB}$ , were used in the calculations, as shown in Table II. By contrast, the actual  $v_s$  was unknown, and the exact TBC could not be estimated. Thus,  $v_s$  was assumed to be  $10\,000 \text{ cm/s}$ , the TBC was calculated, and the effect of  $\theta$  on the TBC was evaluated.

Figure 8 shows the TBC as a function of  $\theta$  when  $v_s$  is  $10\,000 \text{ cm/s}$ . Similar to the with-Al measurement, the w/o-Al measurement also showed that the larger the  $\theta$  value, the larger the TBC, as shown in Fig. 8. To confirm the effect of  $v_s$  on the TBC,  $v_s$  was changed to  $2000$  and  $5000 \text{ cm/s}$ . When  $v_s$  was  $2000$  and  $5000 \text{ cm/s}$ , the TBC slightly decreased, but the relationship in which larger  $\theta$  values yield larger TBCs did not change. The TBC was calculated when changing the carrier lifetime as well. As explained in Sec. II C,  $\tau$  was calculated from the carrier diffusion length obtained via photoluminescence imaging and machine learning. Because the carrier diffusion length varied from  $150$  to  $250 \mu\text{m}$  with an average of  $200 \mu\text{m}$ , the corresponding  $\tau$  could vary from  $22.5$  to  $62.5 \mu\text{s}$  with an average of  $40 \mu\text{s}$ . Calculating TBC with  $\tau$  set to  $22.5$  and  $62.5 \mu\text{s}$  yielded the same results as when a value of  $40 \mu\text{s}$  was used. For both the w/o- and with-Al measurements, the larger the  $\theta$ , the larger the TBC. Therefore, it was confirmed that

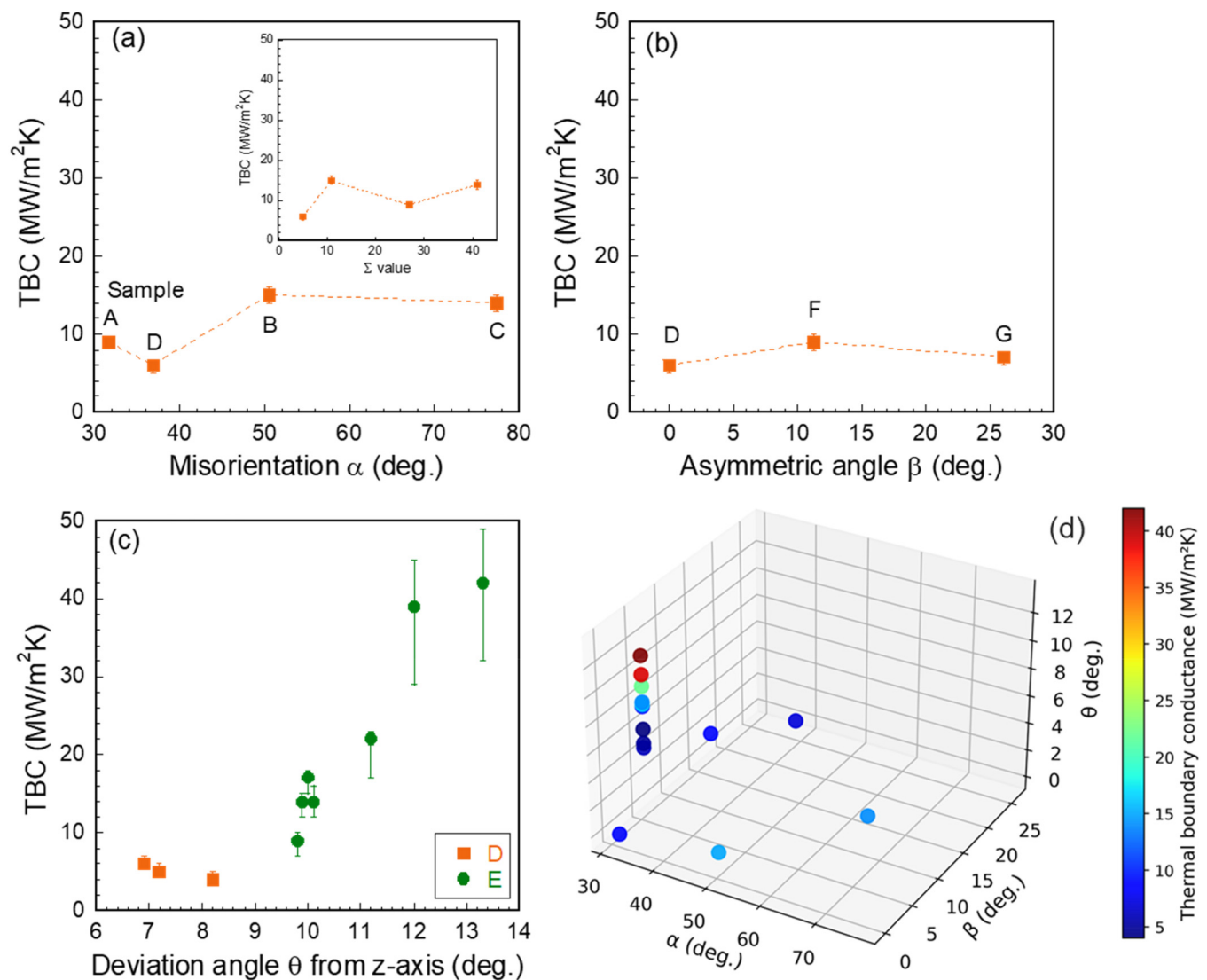


**FIG. 7.** The TBC as a function of three GB parameters: (a) misorientation  $\alpha$  (related to  $\Sigma$  value), (b) asymmetric angle  $\beta$ , and (c) deviation angle  $\theta$  from the z-direction for the with-AI measurement. Because  $\theta$  in samples D and E changed continuously, the TBC was measured at multiple locations in each sample. The result with the smallest  $\theta$  in sample D was used in (a) and (b). (d) The relation between TBC and three GB parameters in three dimensions. Large and small TBCs are shown in red and blue, respectively. (d) is based on the same results as (a)–(c). The error of the TBC was estimated from the experimental error. The time variation of the displacement was measured for 400 000 cycles and averaged. The results in (a) and (b) are averages of measurements taken at two or more locations within the sample. Since  $\theta$  varies depending on the location within the sample, the horizontal axis in (c) results from measurements at different locations.

the TBC at the GB obtained by the with-AI measurements was appropriate.

### C. Relation between $\theta$ and TBC

Considering the cause of a larger TBC with a larger  $\theta$ , we supposed that the carrier concentration and impurity segregation around the GBs should be related to the TBC.  $\theta$  changes the carrier concentration owing to the change in due to the segregation of

impurities, which in turn affects the TBC. The relationships among the carrier concentration, thermal conductivity, and impurity segregation at the GBs are summarized below.

First, we review the relationship between carrier concentration and thermal conductivity of bulk Si. First-principles calculations and experiments show that the thermal conductivity decreases with increasing carrier concentration, and the decrease begins at carrier concentrations around  $10^{17} \text{ cm}^{-3}$ .<sup>37–39</sup> We expect that the change in thermal conductivity with the change



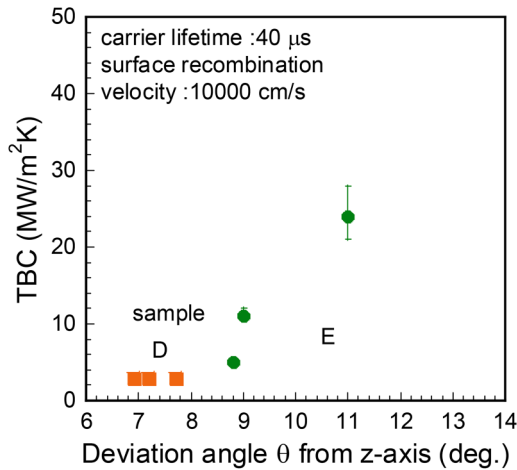


**FIG. 8.** The TBC as a function of the deviation angle  $\theta$  from the z-direction based on the w/o-Al measurements.  $v_{SR}$  was assumed to be 10 000 cm/s. Because  $v_{SR}$  is unknown, the TBC cannot be determined from the w/o-Al measurements. However, a tendency for larger TBCs with larger  $\theta$  values was observed, confirming the validity of the with-Al measurement results. The error of the TBC was estimated in the same way with Fig. 7.

in carrier concentration is related to the relationship between  $\theta$  and TBC in this study.

Dopant segregation in GBs has been reported by many authors. Atom probe tomography has demonstrated that P segregates at the GB in multicrystalline Si.<sup>40,41</sup> The concentration of P was  $2.0 \times 10^{20} \text{ cm}^{-3}$  in the region away from the GB, but  $1.0 \times 10^{21} \text{ cm}^{-3}$  at the GB. In addition, there have been reports of varying amounts of dopant segregation depending on the type of GB.<sup>42</sup> The segregation of the As dopant was highest in the GBs of  $\Sigma 9\{111\}/\{115\}$ , followed by those of  $\Sigma 9\{114\}$ ,  $\Sigma 9\{221\}$ , and  $\Sigma 3\{111\}$  in descending order.<sup>42</sup> This was due to the distortion of the GBs and the formation of a five-membered ring structure at the GBs, which caused dopant segregation.<sup>43</sup> Dopant segregation can vary depending on the structures of the GBs.

Metallic impurities have also been reported to segregate toward GBs. Segregation near GBs has been studied for polycrystalline Si intentionally doped with Cu.<sup>44</sup> Although there was no segregation at the coincidence site lattice  $\Sigma 3$  GB, C and O precipitated at one of the two random grain boundaries, and C and Cu precipitated at the other. The authors suggested that the precipitation of O may have been prevented by the precipitation of Cu. In addition, the GB with segregated C and Cu have had larger boundary recombination velocities than the GB with segregated C and O, indicating that metal segregation leads to larger boundary recombination velocities. Moreover, it has been reported that for a sample with two GB facets, Fe segregated toward both facets, whereas Cu and SiO each precipitated at different facets, and O segregated toward the intersection of the facets.<sup>45</sup> It has been suggested that the type of segregated atoms varies with the GB structures. Although metallic impurities have been reported to be less likely to segregate at lower  $\Sigma$  values, they have been reported to segregate more

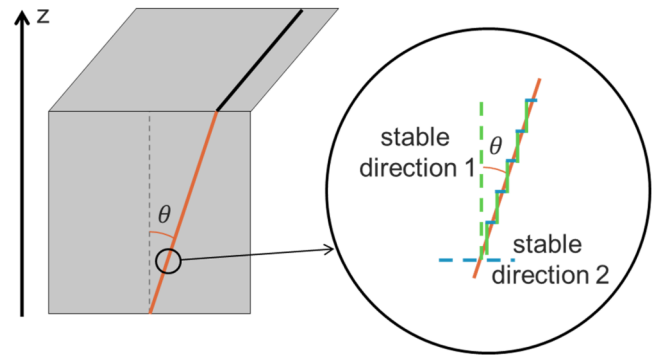


**FIG. 9.** Schematic diagram of GB with macroscopic  $\theta$  and expected microscopic structure. Microscopically, the GB plane has a zigzag shape with the stable surface at the atomic level.

intensively at dislocations.<sup>46,47</sup> It has also been reported that when the GB has a zigzag shape, metallic impurities segregate intensively at the intersections of the facets.<sup>48</sup>

Based on the above report, we discuss the relationship between  $\theta$  and the TBC in this study. We expect a decrease in carrier concentration and high thermal conductivity for large  $\theta$  values to lead to an increase in TBC, and an increase in carrier concentration and low thermal conductivity for small  $\theta$  values, leading to a decrease in the TBC.

During the crystal growth process,  $\theta$  decreases. First, we discuss the case in which  $\theta$  is large. Figure 9 shows the possible microscopic growth of GB structures. The GB grew with a slope of  $\theta$  macroscopically, but its microscopic atomic structure had a faceted zigzag structure with stable surfaces.<sup>48,49</sup> These zigzag facets can intensively segregate metallic impurities.  $v_{GB}$  is larger when  $\theta$  is large, which is also expected to indicate the segregation of metallic impurities.<sup>20</sup> When a larger  $\theta$  has a larger  $v_{GB}$ <sup>20</sup> and carriers are trapped in the GB, the carrier concentration decreases near the GB with a large  $\theta$ . Furthermore, the segregation of metallic impurities at a large  $\theta$  may result in small carrier concentrations with little segregation of P from the example of Cu, preventing O segregation.<sup>44</sup> As mentioned in Sec. II A, the carrier concentration of the samples obtained by the four-point probe method was approximately  $10^{16} \text{ cm}^{-3}$ . Note that this carrier concentration was not obtained at the GB. However, it is expected that the carrier concentration at GBs with large  $\theta$  values would be the same because the segregation of P was lower. When the carrier concentration is low, the thermal conductivity is high.<sup>37–39</sup> Because this result was calculated considering electron–phonon interactions, the TBC may also be large.<sup>38,39</sup>

Next, we discuss the case in which  $\theta$  is small. In this situation,  $v_{GB}$  is small.<sup>20</sup> Thus, less segregation of metallic impurities is expected, and P can be segregated. The carrier concentration near the GB can be higher than  $10^{17} \text{ cm}^{-3}$  owing to P segregation, and the thermal conductivity decreases. If  $\theta$  is small and the carrier concentration at the GB is high, the thermal conductivity and TBC can decrease. In summary, the change in  $\theta$  varied the amount of P and metal impurities that were segregated, which changed  $v_{GB}$ ,

19 May 2025 10:32:58

thereby changing the carrier concentration. The decreased carrier concentration may have increased thermal conductivity, which in turn may have increased the TBC.

Another possible cause of the relationship between  $\theta$  and TBC could be a change in the atomic structure such that TBC would be larger when  $\theta$  is large. To confirm the above hypotheses, a combination of measurements of atomic structures and segregated atoms using transmission electron microscopy and atom probe tomography, as well as molecular dynamics simulations, is required. This will be done in future work.

The GB energy is another possible cause of the relationship between  $\theta$  and TBC. Theoretical calculations report that the TBC is small when the GB energy is large.<sup>10</sup> As the GB energy varies with the atomic structure, the calculations for the GB structures in this study are not straightforward. However, we intuitively expect the GB energy to be large when  $\theta$  is large. Thus, the result should be opposite to that of the present study, in that the TBC should be smaller when  $\theta$  is large. This may be because the theoretical calculations do not consider the effects of impurities. It is suggested that in the presence of impurity segregation, the agreement between theoretical calculations and experimental results may not be straightforward.

#### IV. CONCLUSION

By combining the original crystal growth technique and LH-PD measurements, we could evaluate TBCs with systematically designed GB structures. The advantage of the LH-PD method over other methods is that it can measure sufficient signal intensity even when the distance between the excitation and probe beams is more than several tens of micrometers. This allows us to obtain signals across GB. Two types of experiments, with- and w/o-Al measurements, were performed to confirm our results. The differences between the two measurements are whether the TBC between Al and Si and the photoexcited carriers are considered. The with-Al measurements can be discussed by excluding carrier properties and concentrating on thermophysical properties. The w/o-Al measurement was done to confirm the TBC of GBs since the TBC between Al and Si was small in the with-Al measurement. The TBC of GBs estimated from both measurements showed the same trend. A larger TBC was observed when  $\theta$  was large, whereas  $\alpha$  and  $\beta$  did not affect the TBC. Larger  $\theta$  resulted in larger  $v_{GB}$ <sup>20</sup> and TBC. Both are related to the impurity segregation and following fluctuation of the carrier concentration.

GB segregation engineering is an approach that manipulates the segregation of GBs to achieve desired properties.<sup>45</sup> This has been reported to control parameters such as fracture resistance, electrical conductivity, and resistance to dislocations in structural alloys. If the segregated impurities vary with the angle  $\theta$  and the properties of the GB are changed by segregated impurities, GB engineering could be further improved by controlling  $\theta$ .

The combination of the original crystal growth method and the LH-PD method was shown to be capable of evaluating the TBC of a GB in detail. Since a larger  $\theta$  results in a larger TBC, GBs with a larger  $\theta$  may contribute to heat dissipation. Materials used for heat spreaders and heat sinks may have a good performance due to GBs with large  $\theta$ .

#### ACKNOWLEDGMENTS

We thank H. Tajika (Nagoya University) for assistance with sample preparation. This study was supported by JST, CREST (Grant No. JPMJCR17J1).

#### AUTHOR DECLARATIONS

##### Conflict of Interest

The authors have no conflicts to disclose.

#### Author Contributions

**T. Harada:** Data curation (lead); Formal analysis (lead); Investigation (lead); Methodology (equal); Software (lead); Validation (equal); Visualization (lead); Writing – original draft (lead). **K. Kutsukake:** Conceptualization (equal); Formal analysis (equal); Methodology (equal); Software (equal); Supervision (equal); Validation (equal); Writing – review & editing (equal). **N. Usami:** Conceptualization (equal); Funding acquisition (lead); Methodology (equal); Project administration (equal); Resources (equal); Supervision (equal); Writing – review & editing (equal). **T. Ikari:** Conceptualization (supporting); Investigation (supporting); Methodology (supporting); Supervision (supporting); Validation (equal); Visualization (equal); Writing – review & editing (equal). **A. Fukuyama:** Conceptualization (equal); Funding acquisition (equal); Methodology (equal); Project administration (lead); Supervision (lead); Writing – review & editing (equal).

#### DATA AVAILABILITY

The data that support the findings of this study are available from the corresponding author upon reasonable request.

#### REFERENCES

- <sup>1</sup>K. Yamakoshi, Y. Ohno, K. Kutsukake, T. Kojima, T. Yokoi, H. Yoshida, H. Tanaka, X. Liu, H. Kudo, and N. Usami, “Multicrystalline informatics applied to multicrystalline silicon for unraveling the microscopic root cause of dislocation generation,” *Adv. Mater.* **36**, 2308599 (2024).
- <sup>2</sup>T. Watanabe, “Grain boundary engineering: Historical perspective and future prospects,” *J. Mater. Sci.* **46**, 4095 (2011).
- <sup>3</sup>Z. Yu, P. R. Cantwell, Q. Gao, D. Yin, Y. Zhang, N. Zhou, G. S. Rohrer, M. Widom, J. Luo, and M. P. Harmer, “Segregation-induced ordered superstructures at general grain boundaries in a nickel-bismuth alloy,” *Science* **358**, 97 (2017).
- <sup>4</sup>Y. Nagaoka, M. Suda, I. Yoon, N. Chen, H. Yang, Y. Liu, B. A. Anzures, S. W. Parman, Z. Wang, M. Grünwald, H. M. Yamamoto, and O. Chen, “Bulk grain-boundary materials from nanocrystals,” *Chem* **7**, 509 (2021).
- <sup>5</sup>T. Liu, S. Xia, Q. Bai, B. Zhou, Y. Lu, and T. Shoji, “Evaluation of grain boundary network and improvement of intergranular cracking resistance in 316L stainless steel after grain boundary engineering,” *Materials* **12**, 242 (2019).
- <sup>6</sup>A. Senthamizhan, B. Balusamy, Z. Aytac, and T. Uyar, “Grain boundary engineering in electrospun ZnO nanostructures as promising photocatalysts,” *CrystEngComm* **18**, 6341 (2016).
- <sup>7</sup>J. F. Li, W. S. Liu, L. D. Zhao, and M. Zhou, “High-performance nanostructured thermoelectric materials,” *NPG Asia Mater.* **2**, 152 (2021).
- <sup>8</sup>M. T. Dylla, J. J. Kuo, I. Witting, and G. J. Snyder, “Grain boundary engineering nanostructured SrTiO<sub>3</sub> for thermoelectric applications,” *Adv. Materials Interfaces* **6**, 1900222 (2019).

- <sup>9</sup>S. Fujii and A. Seko, "Structure and lattice thermal conductivity of grain boundaries in silicon by using machine learning potential and molecular dynamics," *Comput. Mater. Sci.* **204**, 111137 (2022).
- <sup>10</sup>J. Hickman and Y. Mishin, "Thermal conductivity and its relation to atomic structure for symmetrical tilt grain boundaries in silicon," *Phys. Rev. Mater.* **4**, 033405 (2020).
- <sup>11</sup>S.-H. Ju and X.-G. Liang, "Investigation on interfacial thermal resistance and phonon scattering at twist boundary of silicon," *J. Appl. Phys.* **113**, 053513 (2013).
- <sup>12</sup>S. Fujii, T. Yokoi, C. A. J. Fisher, H. Moriwake, and M. Yoshiya, "Quantitative prediction of grain boundary thermal conductivities from local atomic environments," *Nat. Commun.* **11**, 1854 (2020).
- <sup>13</sup>M. Sakata, T. Hori, T. Oyake, J. Maire, M. Nomura, and J. Shiomi, "Tuning thermal conductance across sintered silicon interface by local nanostructures," *Nano Energy* **13**, 601–608 (2015).
- <sup>14</sup>D. Xu, R. Hanus, Y. Xiao, S. Wang, G. J. Snyder, and Q. Hao, "Thermal boundary resistance correlated with strain energy in individual Si film-wafer twist boundaries," *Mater. Today Phys.* **6**, 53 (2018).
- <sup>15</sup>D. H. Hurley, M. Khafizov, and S. L. Shinde, "Measurement of the Kapitza resistance across a bicrystal interface," *J. Appl. Phys.* **109**, 083504 (2011).
- <sup>16</sup>K. Tai, A. Lawrence, M. P. Harmer, and S. J. Dillon, "Misorientation dependence of  $\text{Al}_2\text{O}_3$  grain boundary thermal resistance," *Appl. Phys. Lett.* **102**, 034101 (2013).
- <sup>17</sup>E. Isotta, S. Jiang, G. Moller, A. Zevalkink, G. J. Snyder, and O. Balogun, "Microscale imaging of thermal conductivity suppression at grain boundaries," *Adv. Mater.* **35**, 2302777 (2023).
- <sup>18</sup>Y. Fukuda, K. Kutsukake, T. Kojima, and N. Usami, "Effects of grain boundary structure and shape of the solid–liquid interface on the growth direction of the grain boundaries in multicrystalline silicon," *CrystEngComm* **24**, 1948 (2022).
- <sup>19</sup>K. Kutsukake, K. Mitamura, N. Usami, and T. Kojima, "Direct prediction of electrical properties of grain boundaries from photoluminescence profiles using machine learning," *Appl. Phys. Lett.* **119**, 032105 (2021).
- <sup>20</sup>Y. Fukuda, K. Kutsukake, T. Kojima, Y. Ohno, and N. Usami, "Study on electrical activity of grain boundaries in silicon through systematic control of structural parameters and characterization using a pretrained machine learning model," *J. Appl. Phys.* **132**, 025102 (2022).
- <sup>21</sup>T. Harada, T. Ikari, and A. Fukuyama, "Development of laser heterodyne photothermal displacement method for mapping carrier nonradiative recombination centers in semiconductors," *J. Appl. Phys.* **131**, 195701 (2022).
- <sup>22</sup>H. Takamatsu, S. Sumie, T. Morimoto, Y. Kawata, T. Muraki, and T. Hara, *J. Appl. Phys.* **78**, 1504 (1995).
- <sup>23</sup>J. Younes, Z. Harajli, M. Soueidan, D. Fabrègue, Y. Zaatar, and M. Kazan, *J. Appl. Phys.* **127**, 173101 (2020).
- <sup>24</sup>K. Hara and T. Takahashi, *Appl. Phys. Express* **5**, 022301 (2012).
- <sup>25</sup>X. Qian, Z. Ding, J. Shin, A. J. Schmidt, and G. Chen, *Rev. Sci. Instrum.* **91**, 064903 (2020).
- <sup>26</sup>See [www.comsol.com](http://www.comsol.com) for "COMSOL AB, COMSOL Multiphysics® v. 6.1" Stockholm, Sweden.
- <sup>27</sup>A. Pinto Neto, H. Vargas, N. F. Leite, and L. C. M. Miranda, *Phys. Rev. B* **40**, 3924 (1989).
- <sup>28</sup>E. D. Palic, *Handbook of Optical Constants of Solids* (Academic Press, 1985), p. 399.
- <sup>29</sup>F. C. Nix and D. MacNair, "The thermal expansion of pure metals: Copper, gold, aluminum, nickel, and iron," *Phys. Rev.* **60**, 597 (1941).
- <sup>30</sup>E. J. Gonzalez, J. E. Bonevich, G. R. Stafford, G. White, and D. Josell, "Thermal transport through thin films: Mirage technique measurements on aluminum/titanium multilayers," *J. Mater. Res.* **15**, 764 (2000).
- <sup>31</sup>O. Kessler and M. Reich, "Similarities and differences in heat treatment simulation of aluminium alloys and steels," *Materwiss Werksttech* **40**, 473 (2009).
- <sup>32</sup>J. Kováčik, L. Marsavina, and E. Linul, "Poisson's ratio of closed-cell aluminium foams," *Materials* **11**, 1904 (2018).
- <sup>33</sup>S. M. Sze, *Semiconductor Sensors* (Wiley, New York, 1994), pp. 535–536.
- <sup>34</sup>S. M. Sze and K. K. Ng, *Physics of Semiconductor Devices*, 3rd ed. (John Wiley & Sons, Hoboken, 2007), pp. 665–790.
- <sup>35</sup>M. E. Levinstein, S. L. Rumyantsev, and M. S. Shur, *Properties of Advanced Semiconductor Materials: GaN, AlN, InN, BN, SiC, SiGe* (Wiley, New York, 2001), pp. 141–154.
- <sup>36</sup>J. Zhu, D. Tang, W. Wang, J. Liu, K. W. Holub, and R. Yang, "Ultrafast thermoreflectance techniques for measuring thermal conductivity and interface thermal conductance of thin films," *J. Appl. Phys.* **108**, 094315 (2010).
- <sup>37</sup>G. A. Slack, "Thermal conductivity of pure and impure silicon, silicon carbide, and diamond," *J. Appl. Phys.* **35**, 3460 (1964).
- <sup>38</sup>B. Liao, B. Qiu, J. Zhou, S. Huberman, K. Esfarjani, and G. Chen, "Significant reduction of lattice thermal conductivity by the electron-phonon interaction in silicon with high carrier concentrations: A first-principles study," *Phys. Rev. Lett.* **114**, 115901 (2015).
- <sup>39</sup>B. Dongre, J. Carrete, S. Wen, J. Ma, W. Li, N. Mingo, and G. K. H. Madsen, "Combined treatment of phonon scattering by electrons and point defects explains the thermal conductivity reduction in highly-doped Si," *J. Mater. Chem. A Mater* **8**, 1273 (2020).
- <sup>40</sup>S. Duguay, A. Colin, D. Mathiot, P. Morin, and D. Blavette, "Atomic-scale redistribution of dopants in polycrystalline silicon layers," *J. Appl. Phys.* **108**, 034911 (2010).
- <sup>41</sup>H. Takamizawa, Y. Shimizu, K. Inoue, Y. Nozawa, T. Toyama, F. Yano, M. Inoue, A. Nishida, and Y. Nagai, "Predoping effects of boron and phosphorous on arsenic diffusion along grain boundaries in polycrystalline silicon investigated by atom probe tomography," *Appl. Phys. Express* **9**, 106601 (2016).
- <sup>42</sup>Y. Ohno, T. Yokoi, Y. Shimizu, J. Ren, K. Inoue, Y. Nagai, K. Kutsukake, K. Fujiwara, A. Nakamura, K. Matsunaga, and H. Yoshida, "Segregation mechanism of arsenic dopants at grain boundaries in silicon," *Sci. Technol. Adv. Mater. Methods* **1**, 169 (2021).
- <sup>43</sup>D. Zhao and Y. Li, "Revealing the factors influencing grain boundary segregation of P, As in Si: Insights from first-principles," *Acta Mater.* **168**, 52 (2019).
- <sup>44</sup>A. Stoffers, O. Cojocar-Mirédin, W. Seifert, S. Zaefferer, S. Riepe, and D. Raabe, "Grain boundary segregation in multicrystalline silicon: Correlative characterization by EBSD, EBIC, and atom probe tomography," *Prog. Photovoltaics Res. Appl.* **23**, 1742 (2015).
- <sup>45</sup>A. Stoffers, J. Barthel, C. H. Liebscher, B. Gault, O. Cojocar-Mirédin, C. Scheu, and D. Raabe, "Correlating atom probe tomography with atomic-resolved scanning transmission electron microscopy: Example of segregation at silicon grain boundaries," *Microsc. Microanal.* **23**, 291 (2017).
- <sup>46</sup>T. Buonassisi, A. A. Istratov, M. D. Pickett, M. A. Marcus, T. F. Ciszek, and E. R. Weber, "Metal precipitation at grain boundaries in silicon: Dependence on grain boundary character and dislocation decoration," *Appl. Phys. Lett.* **89**, 042102 (2006).
- <sup>47</sup>Y. Ohno, K. Kutsukake, M. Deura, I. Yonenaga, Y. Shimizu, N. Ebisawa, K. Inoue, Y. Nagai, H. Yoshida, and S. Takeda, "Recombination activity of nickel, copper, and oxygen atoms segregating at grain boundaries in mono-like silicon crystals," *Appl. Phys. Lett.* **109**, 142105 (2016).
- <sup>48</sup>C. H. Liebscher, A. Stoffers, M. Alam, L. Lymperakis, O. Cojocar-Mirédin, B. Gault, J. Neugebauer, G. Dehm, C. Scheu, and D. Raabe, "Strain-induced asymmetric line segregation at faceted Si grain boundaries," *Phys. Rev. Lett.* **121**, 015702 (2018).
- <sup>49</sup>D. Raabe, M. Herbig, S. Sandlöbes, Y. Li, D. Tytko, M. Kuzmina, D. Ponge, and P.-P. Choi, "Grain boundary segregation engineering in metallic alloys: A pathway to the design of interfaces," *Curr. Opin. Solid State Mater. Sci.* **18**, 253 (2014).